Lithiation of SiO₂ in Li-Ion Batteries: In Situ Transmission Electron Microscopy Experiments and Theoretical Studies

Yuefei Zhang,[†] Yujie Li,[†] Zhenyu Wang,[†] and Kejie Zhao*[,‡]

[†]Institute of Microstructure and Property of Advanced Materials, Beijing University of Technology, Beijing 100124, People's Republic of China

[‡]School of Mechanical Engineering, Purdue University, West Lafayette, Indiana 47906, United States

 Ⓢ *Supporting Information*

ABSTRACT: Surface passivation has become a routine strategy of design to mitigate the chemomechanical degradation of high-capacity electrodes by regulating the electrochemical process of lithiation and managing the associated deformation dynamics. Oxides are the prevalent materials used for surface coating. Lithiation of SiO₂ leads to drastic changes in its electro-chemo-mechanical properties from an electronic insulator and a brittle material in its pure form to a conductor and a material sustainable of large deformation in the lithiated form. We synthesized SiO₂-coated SiC nanowires that allow us to focus on the lithiation behavior of the sub-10 nm SiO₂ thin coating. We systematically investigate the structural evolution, the electronic conduction and ionic transport properties, and the deformation pattern of lithiated SiO₂ through coordinated in situ transmission electron microscopy experiments, first-principles computation, and continuum theories. We observe the stress-mediated reaction that induces inhomogeneous growth of SiO₂. The results provide fundamental perspectives on the chemomechanical behaviors of oxides used in the surface coating of Li-ion technologies.

KEYWORDS: Surface coating, core–shell, oxides, stress, Li-ion batteries
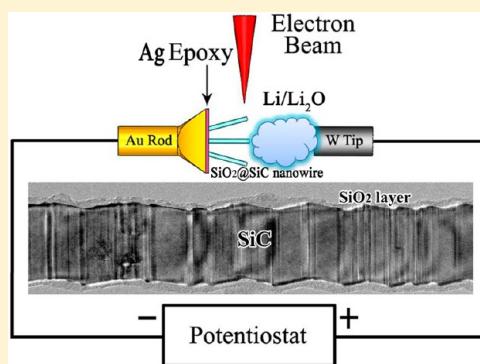
The imperative demand of high-energy-density Li-ion batteries for portable electronics, electric vehicles, and large-scale energy storage stimulated intensive search on the high-capacity electrodes over the past decades.[1,2] A variety of materials have been identified as promising candidates which could potentially boost the energy density up to several times higher over the traditional cells.[3,4] However, the high-capacity electrodes inherently suffer from rapid capacity loss and poor cyclability, primarily due to the mechanical degradation driven by the electrochemical process of lithium insertion/extraction.[5–9] For example, silicon is a leading candidate of high-capacity electrodes to replace the conventional carbon-based anodes. However, its application into commercial batteries is limited by the drastic volumetric deformation during cycles and subsequent mechanical failure.[10] Sulfur offers a theoretical capacity five times higher than the transition-metal based cathodes; however, there is often rapid capacity decay partially resulting from a volumetric strain of 80% upon lithiation.[11] Averting the chemomechanical degradation remains one of the major challenges in the development of high-performance Li-ion batteries.

In recent years, surface passivation has become a routine strategy of design to regulate the electrochemical process of lithiation and mediate the deformation dynamics and fracture pattern, providing a new paradigm to mitigate the mechanical degradation of high-capacity electrodes.[12–15] Oxides are the prevalent materials used for surface coating. Remarkably, silicon anodes coated with a SiO$_x$ native layer can sustain more than 6000 cycles with little capacity fade.[16] Al₂O₃ surface layers grown on Al nanowires can survive 100% volumetric strain with exceptional mechanical robustness.[17] TiO₂ encapsulated sulfur cathodes demonstrated unprecedented cyclability over 1000 cycles.[18] The technique of functional surface coating using oxides opens up pathways for the realization of high-capacity electrodes with sustainable reliability. The improvement via surface passivation is attributed to two major factors. First, the coating materials can effectively alleviate the stress and manage the deformation pattern through geometric constrictions.[13,19] Second, the oxides layer separates the electrodes from direct contacting with the electrolyte, preventing the continual shedding and reforming of solid electrolyte interface (SEI), thus ensuring the maintenance of the electric conduction path for the cell. It is further noteworthy that transition-metal oxides, such as SiO₂, TiO₂, SnO₂, and Co₃O₄, also constitute an important family for high-capacity electrodes; they provide theoretical capacities several times higher than the traditional graphite anodes.[20–22]

However, a fundamental understanding of the electro-chemo-mechanical behaviors of oxides has been largely unexploited. Many intriguing questions arise in the practice
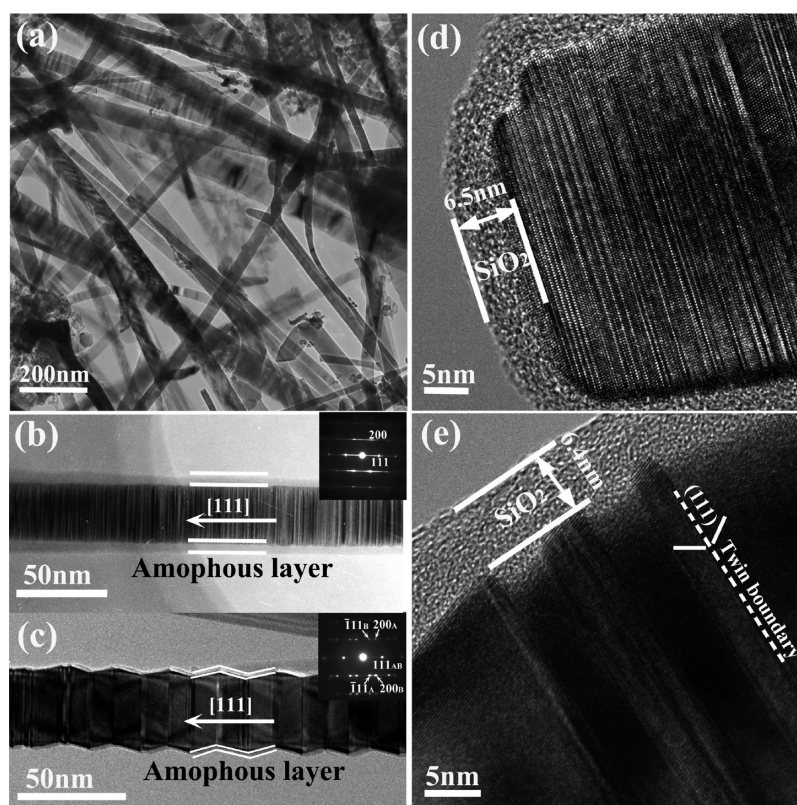
Figure 1. Nanostructure characterization of SiO$_2$-coated SiC (SiO$_2$@SiC) nanowires. (a) Bright-field TEM images. (b) A typical microstructure of SiO$_2$@SiC nanowires with high-density stacking faults along the [111]-growth direction. The streaks shown in the inset SAED indicate high-density stacking faults along the [111] direction. (c) A typical SiO$_2$@SiC nanowire with multiple microtwinning along the growth direction. The inset SAED pattern shows strong diffraction twin spots. The amorphous coating layer of SiO$_2$ in (b,c) are marked by the white lines. (d,e) HRTEM images show sub-10 nm thick SiO$_2$ layer on the surfaces of both stacking-fault and twinning SiC nanowires.
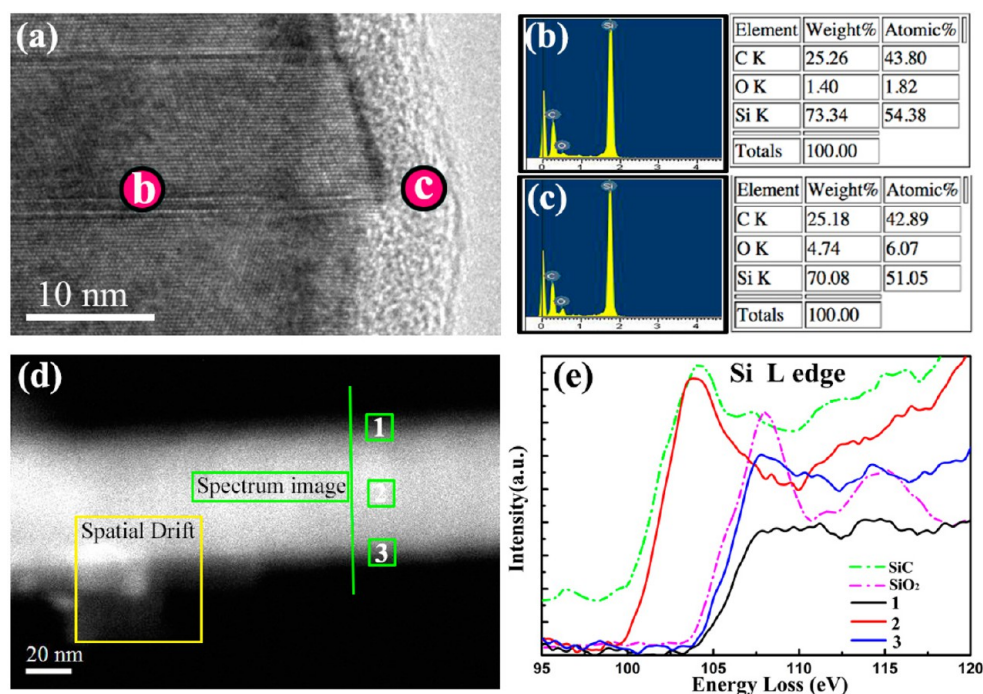

Figure 2. (a) The core−shell structure of SiO$_2$@SiC nanowires. (b,c) The comparison of the EDX spectra acquired from the area "b" in the SiC core and "c" in the SiO$_2$ shell shows more O components in the shell. (d) A STEM-HAADF image of the SiO$_2$@SiC nanowire for EELS line scanning. (e) EELS spectra of Si-L edge measured at the points 1, 2, 3 as marked in the STEM image. The reference Si-L edge spectra in bulk SiO$_2$ and 3C-SiC are shown in the dash-dotted lines. The comparison with the reference spectrum confirms that the composition of the amorphous shell is close to SiO$_2$.
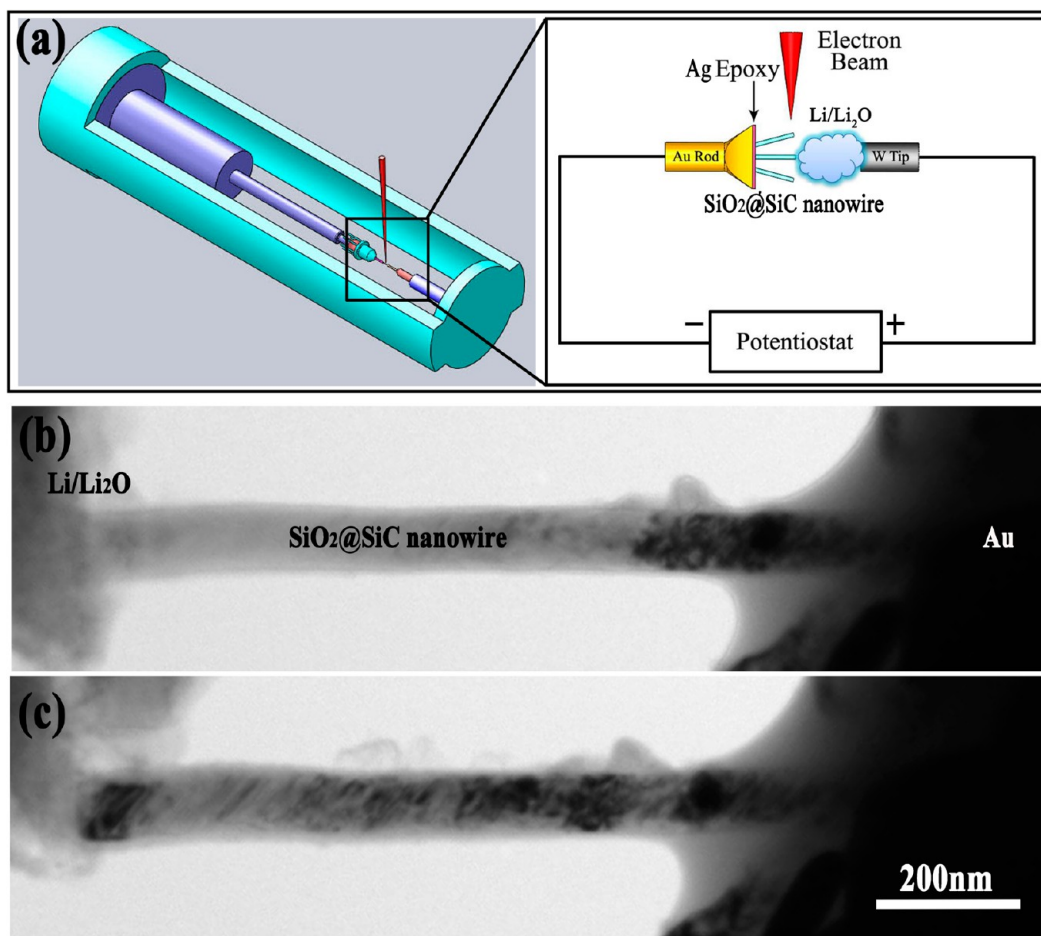
Figure 3. (a) Schematic of a nanobattery consisting of a SiO_2@SiC nanowire as the working electrode, Li/Li$_2$O as the counter electrode and the electrolyte. The Au and W rods are current collectors. (b) A single SiO_2@SiC nanowire integrated in the nanobattery. (c) The morphology change after the first lithiation. Lithiation and delithiation of the nanowire are conducted by applying a bias voltage between the two electrodes. SiC core is inactive to the lithiation reaction.

of Li-ion batteries. For instance, metal oxides are often an insulator of electrons and usually have low permittivity of ions,[23] how does the surface coating remain electronically conductive and allow a fast transport of ions? Oxides are typically brittle materials; they fracture upon loading a small deformation, how does the passivation layer sustain large swelling of 100% strain with superior structural stability? How does a thin coating material influence the electrochemical process of lithiation and remediate the deformation kinetics? How does one rationally design the geometry and pattern of the electrode architecture to reach the optimum chemo-mechanical performance of batteries? While past efforts to address these issues are scattered in literature, few studies systematically investigated the electro-chemo-mechanical behaviors of oxides, especially on the fundamental mechanisms underlying the practice of surface coating. Here, we study the reaction mechanism, the structural evolution, the electronic conduction and ionic transport properties, and the deformation behavior of an example SiO_2 thin layer, through complementary in situ transmission electron microscopy (TEM) experiments, first-principles computation, and continuum theories. We illustrate inhomogeneous growth of the SiO_2 layer mediated by stresses upon lithiation. The present study provides a fundamental understanding on the chemomechanical performance of oxide coating at the intrinsic scales.

We synthesized high-quality SiC nanowires coated with a 2–10 nm thick native SiO_2 layer (SiO_2@SiC) using the sol–gel method followed by thermal reduction.[24−26] SiC is inactive to lithiation, which allows us to focus on the electrochemical behavior of the thin SiO_2 layer. Figure 1a shows the as-synthesized SiC nanowires by the bright-field TEM images. A large number of the products are long and straight with diameters in between 30 and 150 nm, and the length are tens to hundreds of micrometers. As typical features of SiC nanowires, most of the samples present straight high-density stacking faults or zigzag microstructures with multiple microtwinning along the nanowire growth direction, Figure 1b,c. The selected area electron diffraction (SAED) patterns along the [0$\bar{1}$1] direction further confirm the microstructural characteristics. The intense streaks in the stacking direction (inset of Figure 1b) indicate high-density stacking faults along the [111] growth direction of SiC nanowires and the strong diffraction twin spots (inset of Figure 1c indicate the twinning structure. Further structural analysis of the straight and zigzag nanowires is performed by high resolution TEM (HRTEM). Figure 1d,e shows a native grown amorphous SiO_2 layer of sub-10 nm thickness on the surfaces of both stacking-fault and twinning SiC nanowires.

We analyze the chemical composition of SiO_2@SiC nanowires using various techniques. Figure 2a shows a representative HRTEM image of the core–shell structure. The element
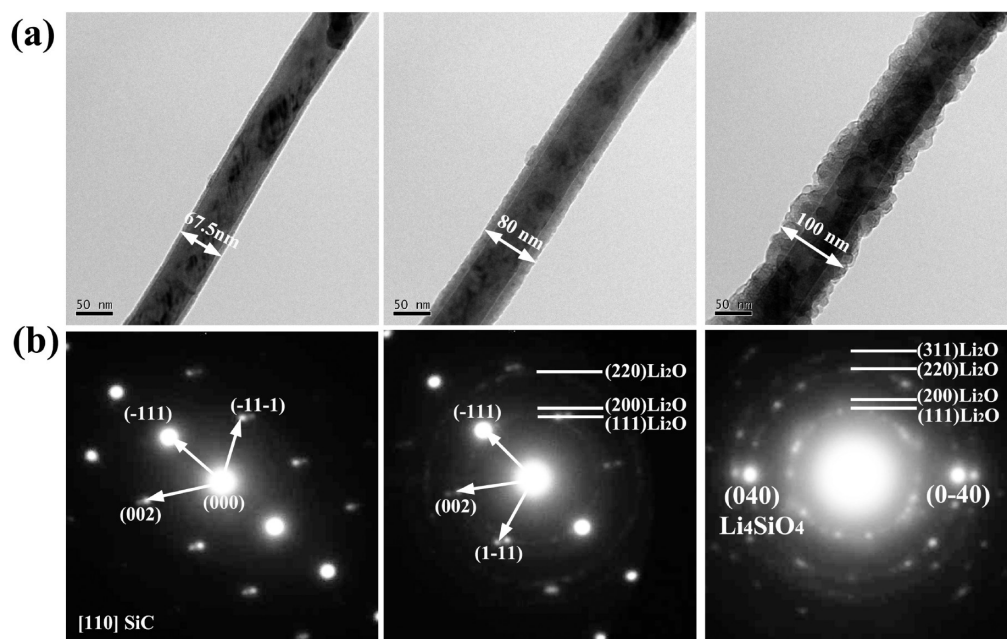
Figure 4. (a) Snapshots of a SiO_2@SiC nanowire from the pristine state to the end of the first lithiation. (b) The corresponding selected area electron diffraction pattern at a given lithiation state in (a). The diffraction spots at the initial state are due to the crystalline SiC core. The lithiation reaction induces a mixture of Li−Si−O glass with Li_4SiO_4 and Li_2O crystalline phases in the shell.

distributions in the marked area "b" in the SiC core and "c" in the SiO_2 shell are mapped using energy dispersive X-ray spectroscopy (EDS). The quantitative results shown in Figure 2b,c indicate more O components in the amorphous shell. To further quantify the chemical formula of the interested thin shell, we collect scanning transmission electron microscope (STEM) images by a high-angle annular dark field detector (HAADF) attached to the JEOL-2010F TEM, Figure 2d. The scanning line for the electron energy loss spectroscopy (EELS) spectrum and the box used for the specimen-drift correction are also marked. Figure 2e shows the comparison of the EELS spectra of Si-L edge acquired from the points 1, 2, 3 along the scanning line across the SiO_2@SiC nanowire. The reference Si-L edge spectra in the bulk SiO_2 and 3C-SiC are also included.[27] It is clear that the shell spectra of the Si-L edges (marked 1 and 3) are significantly different from that acquired from the core region (marked 2). A close comparison with the reference spectra shows the best correspondence of 3C-SiC for the SiC core and SiO_2 for the amorphous shell. The slight difference in the fine structural features between experimental EELS spectrum and the reference may be due to the mixture of signals from the core−shell geometry. We therefore confirm the chemical composition SiO_2 for the amorphous shell, and that little oxygen deficiency is found in the native grown oxide layer.

We integrate a single SiO_2@SiC nanowire into a nanobattery setup and perform in situ electrochemical experiments of lithiation/delithiation. Figure 3a shows the schematic of the experimental setup, consisting of a SiO_2@SiC nanowire as the working electrode, Li/Li_2O as the counter electrode and the electrolyte, and Au and W rods as the current collectors. Lithiation and delithiation are carried out by applying a bias voltage of −5 V and +5 V between the SiO_2@SiC nanowire and the Li counter electrode. A large voltage is necessary to drive the electrochemical reactions because of the small size and poor electronic conductivity of the nanowire. Precautions were taken to avoid the beam effects on lithiation reactions. The in situ experiments are carried out with a low dose rate of electron

flux. During the entire experiments, the electron beam is distributed to a large illumination area with the diameter of 50 μm. We avoid the focus of beams to a small area that may induce undesired radiation effects. Similar experimental setup was also reported by other groups.[28−31] Figure 3b shows the studied nanowire at the initial state. It has a uniform amorphous SiO_2 layer of 5−10 nm thickness coated on the surface. When a bias voltage of −5 V is applied to the nanowire against Li, Figure 3c, only the surface SiO_2 layer is lithiated and the SiC core remains its crystalline structure. This observation indicates that the SiO_2@SiC nanowire is an excellent example system to isolate the electrochemical behaviors of the sub-10 nm amorphous SiO_2 coating layer. The time evolution of a single nanowire upon two cycles of lithiation and delithiation is shown in the Supporting Information Movie S1.

The reaction mechanism between Li and SiO_2 is not well understood. There is still debate on the reaction pathway and final products of the conversion reaction of SiO_2. Early studies believed that SiO_2 was an inert phase to lithiation due to its structural stability that the strong Si−O bonds cannot be broken by the insertion of Li.[32] Thermodynamic calculations also suggested that the driving force for the reduction of SiO_2 to Si and Li_2O was small that the kinetics of the conversion reaction was extremely slow.[33] Therefore, SiO_2 was usually regarded as a mechanical support for the active materials. On the contrary, recent studies claim that reduction of SiO_2 by Li is thermodynamically favorable.[35,36] The general finding is that the electrochemical reduction of nanosized SiO_2 results in possible products of $Li_2Si_2O_5$, Li_4SiO_4, Li_2O, Si, and Li_xSi.[36−43] Some of these phases were proven by solid-state nuclear magnetic resonance (NMR), X-ray photoelectron spectroscopy (XPS), and ex situ HRTEM images.[36,38] Similar reaction products were found for nonstoichoimetric silicon oxides (SiO_x, where $0 < x < 2$) as well.[44−48] Here we examine the phase evolution in the lithiation reaction of the sub-10 nm thick SiO_2 layer using SAED during the in situ experiments. Figure 4a shows the snapshots of the morphology of a SiO_2@SiC

nanowire from the pristine state to the end of the first lithiation. The corresponding SAED pattern is given in Figure 4b. The clear diffraction spots at the initial state are due to the crystalline SiC core. Crystalline Li_2O is formed at the early stage of lithiation. Further reduction reaction induces a mixture of Li−Si−O glass with Li_4SiO_4 and Li_2O crystals in the shell. The crystal structure of Li_4SiO_4 and the simulated diffraction pattern are shown in Supporting Information Figure S1. We do not observe the presence of $Li_2Si_2O_5$ or Li_xSi in their crystalline phases. A closer view in Figure 5a shows the thickness change
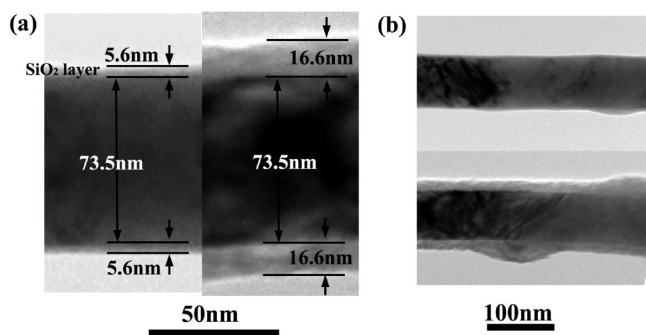

Figure 5. (a) The initial SiO_2 layer with thickness of 5.6 nm grows to 16.6 nm after the first lithiation. (b) Inhomogeneous lithiation of the SiO_2 layer. Lithiated SiO_2 forms a wavy structure that parts of the surface grow thicker than others.

of the nanowire after the first lithiation; the initial SiO_2 layer with thickness of 5.6 nm grows to 16.6 nm that corresponds to a volumetric strain of ca. 200%. In addition, the size of the SiC core does not change upon lithiation, confirming that SiC is inactive to the electrochemical reaction. We further note that lithiation of the SiO_2 thin layer is inhomogeneous, as seen from a view of a lower magnification in Figure 5b. Lithiated SiO_2 forms a wavy structure that parts of the surface grow thicker than others.

Figure 6a shows details of the inhomogeneous growth of the SiO_2 layer in the course of first lithiation and delithiation cycle. Apparently the SiO_2 thin coating of a relatively uniform thickness grows to a wavy morphology. The time evolution of the morphology change is shown in the Supporting Information Movie S2. Such nonuniform deformation pattern has also been observed in other tested nanowires. Supporting Information Figure S2 shows an example of the wavy structure of another nanowire in the first two lithiation cycles. The inhomogeneous growth of SiO_2 may be due to the stress-regulated lithiation reactions. The stress field is modified by the geometry factor of surface curvature. The lithiated phase of convex curvature develops a field of tensile stresses, facilitating lithium transport through the lithiated material and promoting the interfacial reaction at the phase boundary. On the contrary, a material element in the lithiated phase of concave curvature is under a field of compressive stresses, retarding the electrochemical growth of the SiO_2 layer. To illustrate the distinct feature of stresses, we consider SiO_2 spherical particles with convex and concave surface curvatures, Figure 6b. We derive the stress field associated with the surface curvature using the continuum theory of fluid mechanics. We represent a material element by its distance r from the center. During the electrochemical reaction between Li and SiO_2, it forms a core−shell structure of SiO_2−Li_xSiO_2 with the convex surface, and vice versa in the concave case. We first note that the

lithiated phase must rearrange itself through inelastic deformation in order to accommodate the large volumetric strain of 200% upon lithiation. We simulated the mechanical properties of lithiated SiO_2 through modeling of uniaxial deformation using first-principles methods. Details of the computational methods are described in the following section. The stress−strain response curves of four representative Li_xSiO_2 compositions (x represents the atomic ratio of Li and SiO_2) are shown in Supporting Information Figure S3. Both the strength and elastic modulus significantly decrease when the lithium concentration increases. The lithiation-induced softening may enable viscous flow in the lithiation products. Following the Deal-Grove model for thermal oxidation,[49,50] we describe the viscous flow of lithium silicates by the creeping flow and the continuity equations. The creeping flow equation for Li_xSiO_2, reduced by the Navier−Stokes equation, is given by

$$\eta\nabla^2 v = \nabla p \tag{1}$$

where η is viscosity, v is velocity, and p is pressure in the lithiated material. By taking the symmetry into consideration in a spherical coordination, eq 1 can be rewritten as

$$\eta\frac{\partial}{\partial r}\left[\frac{1}{r^2}\frac{\partial(r^2 v)}{\partial r}\right] = \frac{\partial p}{\partial r} \tag{2}$$

The continuity condition states that

$$\frac{\partial \rho}{\partial t} = -\nabla\cdot\rho v \tag{3}$$

If the lithiated phase is assumed to be incompressible, the oxide density ρ is a constant, and the continuity equations can be simplified to

$$\nabla\cdot v = 0. \tag{4}$$

The continuity eq 4 in a spherical coordination is written as

$$\frac{1}{r^2}\frac{\partial(r^2 v)}{\partial r} = 0 \tag{5}$$

The velocity is obtained that $v = \xi/r^2$, where ξ is a velocity constant to be determined by the growth rate of the lithiation reaction at the interface. Substituting v into eq 2 yields

$$p(r) = \text{constant} \tag{6}$$

The pressure p in a spherical coordination takes the average of the normal stresses, $p = -(\sigma_r + 2\sigma_\theta)/3$, where σ_r and σ_θ represent the radial and hoop stress, respectively. The stress components can be written as the summation of the hydrostatic pressure p and deviatoric stresses s, $\sigma_r(r) = -p + s_r(r)$ and $\sigma_\theta(r) = -p + s_\theta(r)$. The deviatoric stresses are defined as

$$s_r(r) = 2\eta\frac{\partial v_r}{\partial r} = -4\eta\frac{\xi}{r^3}$$

$$s_\theta(r) = 2\eta\frac{v_r}{r} = 2\eta\frac{\xi}{r^3} \tag{7}$$

The values of the stress components are determined by the traction-free boundary condition $\sigma(r)|_{r=b} = 0$. It gives
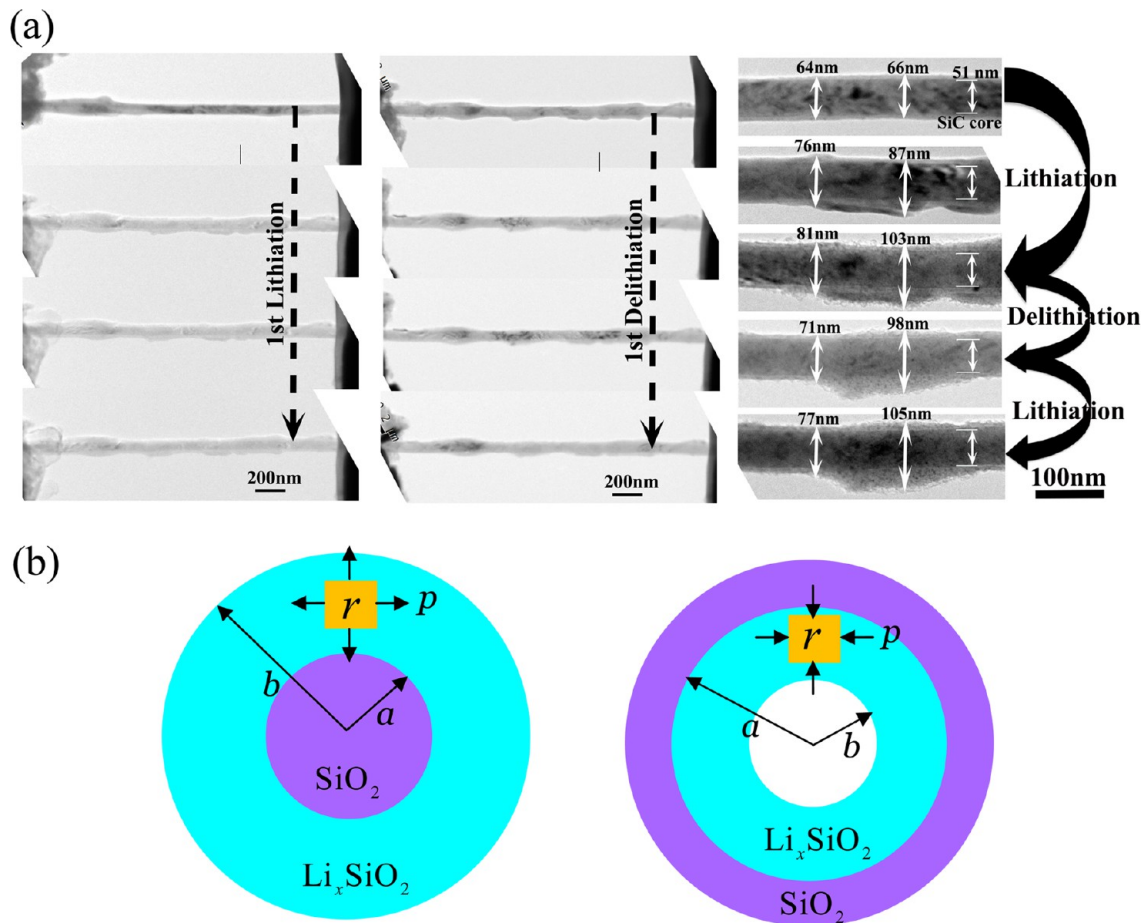
$$p(r) = -4\eta\frac{\xi}{b^3} \tag{8}$$

and

Figure 6. (a) Snapshots of the nonuniform deformation during the first cycle of lithiation and delithiation. (b) Schematic of SiO_2 spherical particles with convex and concave surface curvatures. A material element in the lithiated shell of convex curvature is under a tensile hydrostatic stress, while a material element in the lithiated core of concave curvature is under a compressive hydrostatic stress.

$$\sigma_r(r) = 4\eta\xi\left(\frac{1}{b^3} - \frac{1}{r^3}\right)$$

$$\sigma_\theta(r) = 2\eta\xi\left(\frac{2}{b^3} + \frac{1}{r^3}\right) \quad (9)$$

We see that a constant tensile hydrostatic stress exists in the lithiated shell of convex curvature. A compressive radial stress presents due to the growth of the pristine core, and a tensile hoop stress is due to the lateral stretch of the lithiated shell. If we track the propagation velocity v at the reaction front $r = a$, the velocity constant ξ can be obtained $\xi = v(a)a^2$. It can be further represented by the kinetic parameters in the Deal−Grove model.[50] Similarly, we obtain the stress field in the concave structure

$$p(r) = 4\eta\frac{\xi}{b^3}$$

$$\sigma_r(r) = 4\eta\xi\left(\frac{1}{r^3} - \frac{1}{b^3}\right)$$

$$\sigma_\theta(r) = -2\eta\xi\left(\frac{2}{b^3} + \frac{1}{r^3}\right) \quad (10)$$

It indicates that a material element in the lithiated phase is under a compressive hydrostatic pressure, a tensile radial stress, and a compressive hoop stress.

The presence of hydrostatic stresses can regulate the electrochemical reaction in a significant manner by influencing the kinetics of lithium transport through the lithiated phase, the solid solubility of lithium, and the interfacial reaction at the phase boundary. As evident in a high-resolution image of a SiO_2@SiC nanowire with the twinning microstructure, Supporting Information Figure S4, indeed the SiO_2 layer has alternative convex and concave curvatures. It is plausible that the tensile stress field associated with the convex surface grows a thicker layer of the lithiated phase. Such a stress-mediated reaction provides an interesting mechanism of nonuniform morphology patterns that might be applicable to other electrochemical systems.[51]

We perform atomistic simulations to explore the microscopic mechanism of lithiation in SiO_2. We first generate an amorphous SiO_2 (a-SiO_2) structure containing 96 atoms by quenching a cubic crystalline phase using nonequilibrium molecular dynamics (MD) simulations.[52] The atomic interactions are described by the empirical Tersoff potential.[53] The sample is first annealed at 5000 K for 100 ps and then is gently quenched from 5000 to 0.01 K for 500 ns, corresponding to a quench rate of 10^{10} K/s. The slow quenching process generates an a-SiO_2 structure free of coordination defects, and with a mass density of 2.23×10^3 kg/m³. Such a model system, shown in Figure 7a, is taken as representative of the ideal continuous network that is relevant to the a-SiO_2 structure. We then employ first-principles computational methods to examine the
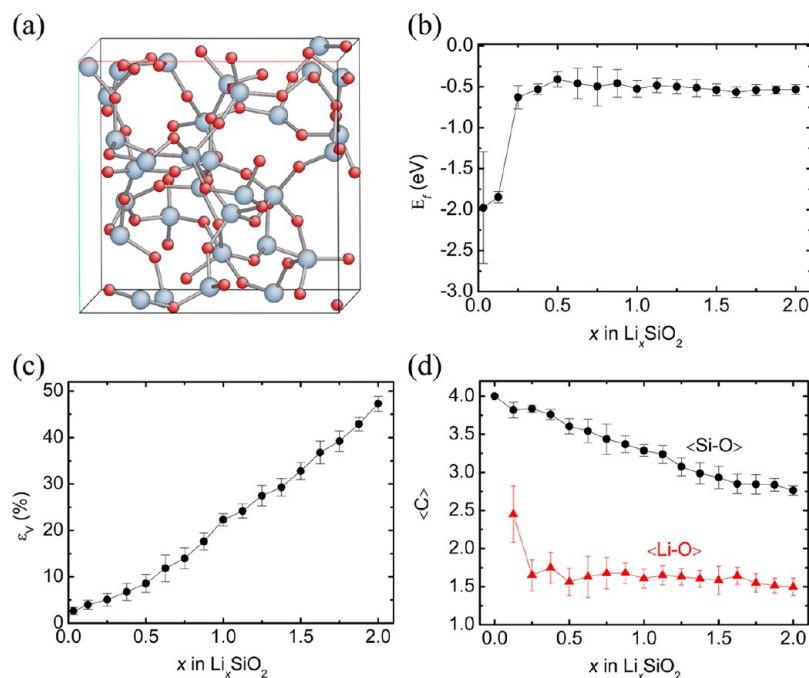
Figure 7. Structural and energetic features of amorphous SiO_2 during lithiation. (a) The atomic configuration of SiO_2 used in first-principles calculations. The gray and red spheres represent the Si and O atoms, respectively. (b) Formation energy per Li in Li_xSiO_2. (c) Volumetric strain. (d) The average values of Si−O coordination and Li−O coordination. The solid lines in the above figures represent the average values from five different configurations of Li_xSiO_2, and the error bars represent the standard deviation at each given Li concentration.

energetics and structural features during lithium insertion into the a-SiO_2 lattice. We incrementally increase Li concentration in the a-SiO_2 network to model the lithiation process. At each Li concentration, we perform the Delaunay triangulation analysis to identify the largest void size in the lattice to accommodate the insertion of Li. Those void spaces are regarded as the general energetically favorable positions for Li insertion. Furthermore, we consider five possible configurations of Li_xSiO_2 at a given Li concentration with different Li distributions in each, to eliminate the large variations inherent to the small model size. We calculate the formation energy per Li at various Li concentrations to study the thermodynamic stability of Li insertion into a-SiO_2. We take the energy of SiO_2 (E_{SiO2}) and the energy of a Li atom in its bulk form (E_{Li}) as the reference energies, with $E_{nLi-SiO2}$ being the total energy of the system containing n Li atoms in the cell. The formation energy per Li atom $E_f(n)$ is calculated as $E_f(n) = [E_{nLi-SiO2} - E_{SiO2} - nE_{Li}]/n$. Figure 7b shows the computational data with the solid symbols representing the average values of the formation energy per Li from five different configurations of Li_xSiO_2, and error bars representing the standard deviation. It is evident that lithiation of a-SiO_2 is energetically favorable with a formation energy of −1.97 eV for 1 Li, −1.85 eV for $Li_{0.0625}SiO_2$, and in the vicinity of −0.5 eV for a wide range of higher Li concentrations. Further increasing Li concentration requires much more intensive computational efforts; here we limit our simulations to Li_2SiO_2 that constitutes 160 atoms in total. Figure 7c shows the evolution of volumetric strain as a function of the Li concentration. The slope of the volumetric strain remains an almost constant throughout the entire range of lithiation. We fit the dependence of the volumetric strain on Li concentration using a linear function, and obtain the partial molar volume of Li in SiO_2 as $\Omega_{Li\ in\ SiO2} = 9.82\ \text{Å}^3$. The large volumetric deformation in a-SiO_2 during Li insertion is accommodated by the gradual rearrangement of the lattice

structure through Si−O bond breaking and Li−Si−O cluster reforming. To examine the bonding mechanism, we measure the evolution of the atomic coordination at various Li concentrations. A physically meaningful measure of atomic coordination is needed to define the atomic bonds. We define Si−O atoms to be bonded if their distance is within 15% of the covalent length in the bulk crystal SiO_2, which corresponds to the largest bond distance of 1.87 Å. Likewise, we define an O atom as bonded with a Li atom if their value is smaller than 2.15 Å, a value taken from the Li−O bond length in lithium silicates of $Li_2Si_2O_5$ and Li_4SiO_4.[36] Figure 7d shows the average values of Si−O coordination ⟨Si−O⟩ and Li−O coordination ⟨Li−O⟩ as a function of the Li composition. The Si−O coordination steadily decreases and changes almost linearly, which indicates a constant rate of Si−O bond breaking. Nevertheless, the Si−O coordination number remains about 3.0 in Li_2SiO_2 that a fair amount of well-defined Si−O bonds still exists and spans the size of the cell. It might be indicative that the formation of Li−Si−O clusters is more energetically favorable compared to the reduction of SiO_2 to Si. More interestingly, the Li−O coordination maintains an almost constant of ca. 1.5 for a wide range of Li contents. It might indicate the presence of local characteristics of Li_2O upon lithium insertion into SiO_2.

The electronic property of the surface coating is crucially important as oxides are often insulator to electrons in the pristine state. To enable a proper function of the passivation layer the electron conduction path must be maintained under the working conditions of batteries. Previous studies suggested that a SiO_2 layer of ca. 7 nm demonstrated the best performance for Si electrodes in the electrochemical cycles,[42] and thicker coating of native SiO_2 layers may prevent the electrode from complete lithiation.[37] Meanwhile, it is noteworthy that insertion of Li could drastically alter the electronic properties of the electrodes, for example, silicon experiences a

transition from the semiconductor state to a metallic state after a small amount of Li is alloyed with silicon.[54] On the basis of first-principles modeling, we study the density of states (DOS) as a measure of the electronic property of amorphous Li_xSiO_2. Figure 8a shows the DOS at four representative Li
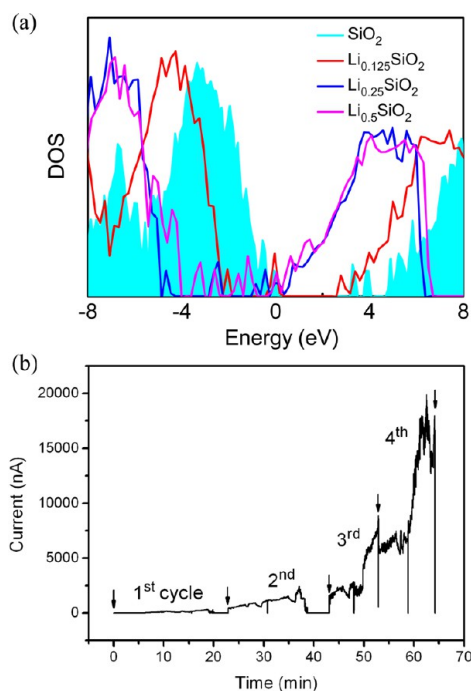

Figure 8. (a) Density of states of Li_xSiO_2 based on first-principles calculations. (b) Measurement of the current in a single SiO_2@SiC nanowire during in situ lithiation/delithiation cycles. Lithiation and delithiation are performed by applying a constant bias voltage of −5 V and +5 V on the SiO_2@SiC nanowire against the Li counter electrode.

concentrations, pristine SiO_2, $Li_{0.125}SiO_2$, $Li_{0.25}SiO_2$, and $Li_{0.5}SiO_2$. The Fermi energies have been shifted to zero of the energy scale. The corresponding DOS of pure SiO_2 has a clear insulator character with a band gap of ca. 3.5 eV. As the concentration of Li increases, Li donates electrons and the band gap significantly decreases. A clear transition of insulator to conductor occurs with more electronic states introduced around the Fermi energy level. On the experimental side, we measure the current that flows through a single SiO_2@SiC nanowire using an ampermeter during in situ cycles of lithiation and delithiation. Figure 8b shows the current measurements in five cycles. It is seen that the current increases dramatically after a few lithiation cycles, representing an increase of the electronic conductivity of SiO_2 upon Li insertion. It should be noted that the experimentally measured current density is a net outcome of several reaction products shown in Figure 4 and is dependent on the length of the nanowire. Such a complication causes the difference between the experimental observations and first-principles predictions. However, a general conclusion is that the electronic conduction of the SiO_2 coating is significantly improved during lithiation/delithiation cycles, which attributes to the high performance of electrodes at fast charging rates.

We also study the kinetics of Li transport through the a-SiO_2 layer. To compute the diffusivity of Li at the temperature of interest, we perform nonequilibrium finite temperature MD simulations within the framework of density functional theory.

The MD calculations are performed at temperatures of 1000, 1500, 2000, and 2500 K. Starting from the relaxed initial configurations, the cells were allowed to dynamically equilibrate at fixed temperatures for roughly 7500 time steps, where each MD step is set as 2 fs. The total simulation time corresponds to 15 ps, which induces substantial mixing of atoms with each other. The random walking of Li is closely examined and the atomic motions are far beyond the local elementary hopping. We calculate the mean square displacements (MSD) for Li, by the definition $MSD = \langle |r_i(t) - r_i(0)|^2 \rangle$, where $r_i(t)$ is the position of the atom i at the time t, $r_0(t)$ is the position of the atom i in the initial configuration, and $\langle \cdot \rangle$ represents an average over the ensemble of atoms. The calculated mean square displacements of Li in six lithium silicates, $Li_{0.125}SiO_2$, $Li_{0.25}SiO_2$, $Li_{0.5}SiO_2$, $LiSiO_2$, $Li_{1.5}SiO_2$, and Li_2SiO_2, are shown in Supporting Information Figure S5. The diffusivity of Li can be derived from the MSD, $D = \lim_{t\to\infty} 1/6t \langle |r_i(t) - r_i(0)|^2 \rangle$. We calculate the diffusivity of Li for different temperatures and extrapolate the data to obtain the diffusivity at $T = 300$ K. The extrapolation is carried out by following the standard expression for diffusivity, $D = D_0 \exp(-E_a/kT)$, where E_a is the energy barrier, k is the Boltzmann constant, and T is the temperature. Plots of diffusivity of Li versus 1000/T on a log scale in the six representative compositions are shown in Supporting Information Figure S6. We also consider the stress effect on Li diffusion.[55] Supporting Information Figure S7 shows the stress fluctuation in the supercell of $Li_{0.5}SiO_2$ at various temperatures. The average values of pressure are about zero for the entire MD simulations. Therefore, the stress effect on Li diffusion is neglected. Figure 9 summarizes the compositional dependence
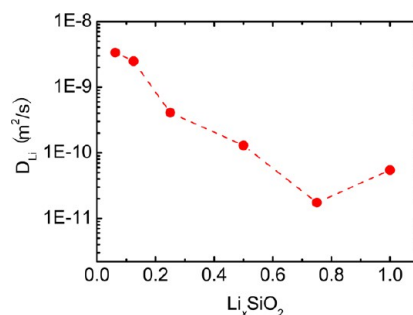

Figure 9. Li diffusivity in Li_xSiO_2 at $T = 300$ K calculated from ab initio molecular dynamic simulations. The solid symbols are calculated data, and the dashed line is a guide for the eyes.

of diffusivity of Li. We see that Li diffuse slower in the lithiated products, and the diffusivity decreases by roughly 2 orders of magnitude along with the Li concentration. It indicates that the reaction products of lithium silicates are poor ionic conductors, consistent with the previous experimental observation.[42] A thin layer of SiO_2 coating is necessary to enable a fast transport of Li during the cycles of lithiation and delithiation. An optimum design of the geometry and size of SiO_2 passivation layer should consider the concurrent effects of lithiation on the electronic conduction and ionic transport.

In conclusion, we synthesized high-quality SiO_2 coated SiC nanowires that allow us to investigate the lithiation mechanism of the thin SiO_2 layer. The sub-10 nm thick oxide is particularly relevant to the recent design strategy of surface passivation in Li-ion technologies. We systematically study the structural evolution, the deformation pattern, the electronic conduction and Li transport properties of SiO_2 in the cycles of lithiation

and delithiation, through complementary in situ TEM experiments, first-principles computation, and continuum theories of fluid mechanics. We observe the lithiation products as a mixture of Li−Si−O glass, crystal Li_4SiO_4, and Li_2O. We analyze the stress effect on the inhomogeneous growth of SiO_2 upon lithiation, the tensile stress in the lithiated phase of convex surface curvature may promote lithiation at a faster rate. Such an observation may provide a mechanism of nonuniform deformation in other electrochemical systems. We further study the thermodynamic stability of lithiation in SiO_2, and illustrate that such a reaction is indeed energetically favorable. Consistent with experimental measurements, we find that electronic conduction of SiO_2 is significantly improved upon lithiation. Li diffusivity however decreases in the form of lithium silicates and may impede battery cells from fast cycles. The experimental visualization and theoretical studies provide significant insights on the optimum design of surface coating in the technologies of Li-ion batteries.

Experimental Section. *Material Synthesis.* The synthesis process of SiO_2@SiC NWs was reported in our previous studies,[24−26] which includes the xerogel preparation and a subsequent carbothermal reduction. First, 6 g of phenolic resin and 0.5 g of lanthanum nitrate were dissolved in 18 mL of ethanol (AR) and then mixed with 25 mL of tetraethoxysilane (TEOS, AR). Then, 0.5 mL of hydrochloric acid was added into the mixture, and the mixture was stirred for up to 30 h to enhance the hydrolysis of TEOS. Finally, 5 mL of hexamethylenetetramine (HMTA, 35.8%) aqueous solution was added into the above mixture for a rapid gelation. The xerogel was obtained by drying the gel product at 110 °C for 12 h. The carbothermal reduction was conducted in a horizontal alumina tubular furnace. The xerogel was heated in Ar (flow rate 60 cm^3/min) to 1020 °C at a rate of 10 °C/min, then to 1320 °C at a rate of 2 °C/min and maintained at this temperature for 6 h. The raw product was heated in air at 700 °C for 4 h to remove the residual carbon, and subsequently treated by nitric acid (HNO_3) to eliminate the impurities. We did not use hydrofluoric acid (HF) in order to maintain the natural SiO_2 coating on SiC NWs surface. A light-green powder (SiO_2@SiC NWs) was obtained after washing in distilled water.

Characterization of SiO_2@SiC NWs by TEM, EDS, and EELS. High-resolution electron microscopy (HREM) and scanning TEM (STEM) with a HADDF detector were conducted using a JEOL-2010F TEM operating at 200 kV. The point resolution was 0.19 nm. The chemical composition of the samples was detected using energy dispersive X-ray spectroscopy (EDS, Oxford Instruments) and electron energy loss spectroscopy (EELS) with a Gatan Enfina PEELS system operating at 200 kV. The energy resolution of the EELS system is about 1.2 eV.

In Situ Experiments. The in situ TEM observations were carried out using the Nanofactory TEM-scanning tunneling microscopy (STM) holder inside a JEOL-2010F TEM. A few SiO_2@SiC NWs were attached to a gold (Au) rod with conductive silver epoxy as the anode. Li metal was scratched by an electrochemically shaped tungsten (W) tip inside a glovebox. The Au and W wires were mounted on the station of TEM-STM holder. The assembly holder was loaded into the TEM chamber within a sealed plastic bag with an air exposure time less than 5 s. By manipulating the pizeo-driven stage with nanometer precision on the TEM-STM holder, the Li_2O covered Li metal electrode came into contact with the single SiO_2@SiC NW. Once a reliable contact was made, a negative or

positive voltage bias was applied to drive the lithiation and delithiation reaction of the SiO_2@SiC NW.

Atomistic Modeling. The first-principles calculations based on density functional theory calculations are performed using Vienna Ab-initio Simulation Package. Projector-augmented-wave potentials are used to mimic the ionic cores, while the generalized gradient approximation in the Perdew−Burke−Ernzerhof flavor is employed for the exchange and correlation functional.[56,57] In particular, we treat $1s^2 2s^1$ orbitals as the valence configuration for Li. The atomic structures and system energy are calculated with an energy cutoff of 500 eV. For Brillouin zone sampling, a $2 \times 2 \times 2$ mesh of k-points in the Monkhorst−Pack scheme is sufficient in the energetic relaxation of a-Li_xSiO_2. We use a $1 \times 1 \times 1$ mesh of k-points in the ab initio molecular dynamics simulations. The energy optimization was considered complete when the magnitude of the force on each atom was smaller than 0.02 eV $Å^{-1}$.

■ ASSOCIATED CONTENT

ⓢ Supporting Information
Additional figures and two movie files showing (Movie S1) the time evolution of a single nanowire upon two cycles of lithiation and delithiation and (Movie S2) inhomogeneous growth of the SiO_2 thin layer upon two cycles of lithiation and delithiation. This material is available free of charge via the Internet at http://pubs.acs.org.

■ AUTHOR INFORMATION

Corresponding Author
*E-mail: kjzhao@purdue.edu.
Notes
The authors declare no competing financial interest.

■ ACKNOWLEDGMENTS

■ REFERENCES

(1) Service, R. F. *Science* **2014**, *344*, 352−354.
(2) Van Noorden, R. *Nature* **2014**, *507*, 26−28.
(3) Yu, H. C.; Ling, C.; Bhattacharya, J.; Thomas, J. C.; Thornton, K.; Van der Ven, A. *Energy Environ. Sci.* **2014**, *7*, 1760−1768.
(4) Goodenough, J. B.; Park, K. S. *J. Am. Chem. Soc.* **2013**, *135*, 1167−1176.
(5) Choi, N. S.; Yao, Y.; Cui, Y.; Cho, J. *J. Mater. Chem.* **2011**, *21*, 9825−9840.
(6) Zhang, W. J. *J. Power Sources* **2011**, *196*, 13−24.
(7) Zhao, K. J.; Pharr, M.; Vlassak, J. J.; Suo, Z. G. *J. Appl. Phys.* **2010**, *108*, 073517.
(8) Yang, H.; Fan, F.; Liang, W.; Guo, X.; Zhu, T.; Zhang, S. *J. Mech. Phys. Solids* **2014**, *70*, 349−361.
(9) Zhao, K. J.; Pharr, M.; Vlassak, J. J.; Suo, Z. G. *J. Appl. Phys.* **2011**, *109*, 016110.
(10) Mukhopadhyay, A.; Sheldon, B. W. *Prog. Mater. Sci.* **2014**, *63*, 58−116.
(11) Zheng, G. Y.; Yang, Y.; Cha, J. J.; Hong, S. S.; Cui, Y. *Nano Lett.* **2011**, *11*, 4462−4467.

(12) Marichy, C.; Bechelany, M.; Pinna, N. *Adv. Mater.* **2012**, *24*, 1017−1032.

(13) McDowell, M. T.; Lee, S. W.; Ryu, I.; Wu, H.; Nix, W. D.; Choi, J. W.; Cui, Y. *Nano Lett.* **2011**, *11*, 4018−4025.

(14) Zhao, K.; Pharr, M.; Hartle, L.; Vlassak, J. J.; Suo, Z. *J. Power Sources* **2012**, *218*, 6−14.

(15) Sandu, G.; Brassart, L.; Gohy, J.-F.; Pardoen, T.; Melinte, S.; Vlad, A. *ACS Nano* **2014**, *8*, 9427−9436.

(16) Wu, H.; Chan, G.; Choi, J. W.; Ryu, I.; Yao, Y.; McDowell, M. T.; Lee, S. W.; Jackson, A.; Yang, Y.; Hu, L. B.; Cui, Y. *Nat. Nanotechnol.* **2012**, *7*, 309−314.

(17) Liu, Y.; Hudak, N. S.; Huber, D. L.; Limmer, S. J.; Sullivan, J. P.; Huang, J. Y. *Nano Lett.* **2011**, *11*, 4188−4194.

(18) Seh, Z. W.; Li, W. Y.; Cha, J. J.; Zheng, G. Y.; Yang, Y.; McDowell, M. T.; Hsu, P. C.; Cui, Y. *Nat. Commun.* **2013**, *4*, 1331.

(19) Hertzberg, B.; Alexeev, A.; Yushin, G. *J. Am. Chem. Soc.* **2010**, *132*, 8548−8549.

(20) Huang, J. Y.; Zhong, L.; Wang, C. M.; Sullivan, J. P.; Xu, W.; Zhang, L. Q.; Mao, S. X.; Hudak, N. S.; Liu, X. H.; Subramanian, A.; Fan, H. Y.; Qi, L. A.; Kushima, A.; Li, J. *Science* **2010**, *330*, 1515−1520.

(21) Favors, Z.; Wang, W.; Bay, H. H.; George, A.; Ozkan, M.; Ozkan, C. S. *Sci. Rep.* **2014**, *4*, 4605.

(22) Tao, L. Q.; Zai, J. T.; Wang, K. X.; Zhang, H. J.; Xu, M.; Shen, J.; Su, Y. Z.; Qian, X. F. *J. Power Sources* **2012**, *202*, 230−235.

(23) Glass, A. M.; Nassau, K. *J. Appl. Phys.* **1980**, *51*, 3756−3761.

(24) Dong-Hua, W.; Di, X.; Qing, W.; Ya-Juan, H.; Guo-Qiang, J.; Xiang-Yun, G.; Tu, K. N. *Nanotechnology* **2008**, *19*, 215602.

(25) Hao, Y.-J.; Jin, G.-Q.; Han, X.-D.; Guo, X.-Y. *Mater. Lett.* **2006**, *60*, 1334−1337.

(26) Zhang, Y. F.; Han, X. D.; Zheng, K.; Zhang, Z.; Zhang, X. N.; Fu, J. Y.; Ji, Y.; Hao, Y. J.; Guo, X. Y.; Wang, Z. L. *Adv. Funct. Mater.* **2007**, *17*, 3435−3440.

(27) Zhou, W.; Kapetanakis, M. D.; Prange, M. P.; Pantelides, S. T.; Pennycook, S. J.; Idrobo, J.-C. *Phys. Rev. Lett.* **2012**, *109*, 206803.

(28) Karki, K.; Zhu, Y. J.; Liu, Y. H.; Sun, C. F.; Hu, L. B.; Wang, Y. H.; Wang, C. S.; Cumings, J. *ACS Nano* **2013**, *7*, 8295−8302.

(29) Gu, M.; Wang, Z. G.; Connell, J. G.; Perea, D. E.; Lauhon, L. J.; Gao, F.; Wang, C. M. *ACS Nano* **2013**, *7*, 6303−6309.

(30) McDowell, M. T.; Lee, S. W.; Harris, J. T.; Korgel, B. A.; Wang, C. M.; Nix, W. D.; Cui, Y. *Nano Lett.* **2013**, *13*, 758−764.

(31) Wang, J. W.; He, Y.; Fan, F. F.; Liu, X. H.; Xia, S. M.; Liu, Y.; Harris, C. T.; Li, H.; Huang, J. Y.; Mao, S. X.; Zhu, T. *Nano Lett.* **2013**, *13*, 709−715.

(32) Huang, H.; Kelder, E. M.; Chen, L.; Schoonman, J. *J. Power Sources* **1999**, *81*, 362−367.

(33) Saint, J.; Morcrette, M.; Larcher, D.; Laffont, L.; Beattie, S.; Peres, J. P.; Talaga, D.; Couzi, M.; Tarascon, J. M. *Adv. Funct. Mater.* **2007**, *17*, 1765−1774.

(34) Guo, B. K.; Shu, J.; Wang, Z. X.; Yang, H.; Shi, L. H.; Liu, Y. N.; Chen, L. Q. *Electrochem. Commun.* **2008**, *10*, 1876−1878.

(35) Ban, C. M.; Kappes, B. B.; Xu, Q.; Engtrakul, C.; Ciobanu, C. V.; Dillon, A. C.; Zhao, Y. F. *Appl. Phys. Lett.* **2012**, *100*, 243905.

(36) Chou, C. Y.; Hwang, G. S. *Chem. Mater.* **2013**, *25*, 3435−3440.

(37) Xun, S.; Song, X.; Wang, L.; Grass, M. E.; Liu, Z.; Battaglia, V. S.; Liu, G. *J. Electrochem. Soc.* **2011**, *158*, A1260−A1266.

(38) Chang, W. S.; Park, C. M.; Kim, J. H.; Kim, Y. U.; Jeong, G.; Sohn, H. J. *Energy Environ. Sci.* **2012**, *5*, 6895−6899.

(39) Song, K.; Yoo, S.; Kang, K.; Heo, H.; Kang, Y. M.; Jo, M. H. *J. Power Sources* **2013**, *229*, 229−233.

(40) Zhang, L.; Deng, J. W.; Liu, L. F.; Si, W. P.; Oswald, S.; Xi, L. X.; Kundu, M.; Ma, G. Z.; Gemming, T.; Baunack, S.; Ding, F.; Yan, C. L.; Schmidt, O. G. *Adv. Mater.* **2014**, *26*, 4527−4532.

(41) Yan, N.; Wang, F.; Zhong, H.; Li, Y.; Wang, Y.; Hu, L.; Chen, Q. W. *Sci. Rep.* **2013**, *3*, 1568.

(42) Sim, S.; Oh, P.; Park, S.; Cho, J. *Adv. Mater.* **2013**, *25*, 4498−4503.

(43) Yoo, H.; Lee, J. I.; Kim, H.; Lee, J. P.; Cho, J.; Park, S. *Nano Lett.* **2011**, *11*, 4324−4328.

(44) Yang, J.; Takeda, Y.; Imanishi, N.; Capiglia, C.; Xie, J. Y.; Yamamoto, O. *Solid State Ionics* **2002**, *152*, 125−129.

(45) Nagao, Y.; Sakaguchi, H.; Honda, H.; Fukunaga, T.; Esaka, T. *J. Electrochem. Soc.* **2004**, *151*, A1572−A1575.

(46) Miyachi, M.; Yamamoto, H.; Kawai, H.; Ohta, T.; Shirakata, M. *J. Electrochem. Soc.* **2005**, *152*, A2089−A2091.

(47) Kim, T.; Park, S.; Oh, S. M. *J. Electrochem. Soc.* **2007**, *154*, A1112−A1117.

(48) Hwa, Y.; Park, C. M.; Sohn, H. J. *J. Power Sources* **2013**, *222*, 129−134.

(49) Deal, B. E.; Grove, A. S. *J. Appl. Phys.* **1965**, *36*, 3770−3778.

(50) Kao, D.-B.; McVittie, J. P.; Nix, W. D.; Saraswat, K. C. *IEEE Trans. Electron Devices* **1988**, *35*, 25−37.

(51) Gu, M.; Yang, H.; Perea, D. E.; Zhang, J.-G.; Zhang, S.; Wang, C.-M. *Nano Lett.* **2014**, *14*, 4622−4627.

(52) Plimpton, S. *J. Comput. Phys.* **1995**, *117*, 1−19.

(53) Munetoh, S.; Motooka, T.; Moriguchi, K.; Shintani, A. *Comput. Mater. Sci.* **2007**, *39*, 334−339.

(54) Zhao, K. J.; Tritsaris, G. A.; Pharr, M.; Wang, W. L.; Okeke, O.; Suo, Z. G.; Vlassak, J. J.; Kaxiras, E. *Nano Lett.* **2012**, *12*, 4397−4403.

(55) Johari, P.; Qi, Y.; Shenoy, V. B. *Nano Lett.* **2011**, *11*, 5494−5500.

(56) Kresse, G.; Furthmüller, J. *Phys. Rev. B* **1996**, *54*, 11169.

(57) Kresse, G.; Joubert, D. *Phys. Rev. B* **1999**, *59*, 1758.